Article

Not peer-reviewed version

# Anion Doping of Tungsten Oxide with Nitrogen: Reactive Magnetron Synthesis, Crystal Structure, Valence Composition, and Optical Properties

Insaf F. Malikov , Nikolay M. Lyadov , Myakzyum Kh. Salakhov , Lenar R. Tagirov *

Posted Date: 28 November 2023

doi: 10.20944/preprints202311.1755.v1

Keywords: electrochromism; tuhgsten trioxide; nitrogen doping; optical transmittance; spectroscopical ellipsometry doi:10.20944/preprints202311.1755.v1

*Article*

# Anion Doping of Tungsten Oxide with Nitrogen: Reactive Magnetron Synthesis, Crystal Structure, Valence Composition, and Optical Properties

**Insaf F. Malikov [1,2], Nikolay M. Lyadov [1], Myakzyum Kh. Salakhov [2] and Lenar R. Tagirov [1,*]**

[1] Zavoisky Physical-Technical Institute, FRC KazSC of RAS, Kazan, Russia; insaf.malikov@gmail.com (I.F.M.); nik061287@mail.ru (N.M.L.)
[2] Institute of Physics, Kazan Federal University, Kazan, Russia; mkhsalakhov@gmail.com
* Correspondence: ltagirov@mail.ru; Tel.: +7-937-592-6758

**Abstract:** Anion doping of tungsten trioxide by nitrogen is used to obtain electrochrome cathode material, the spectral transmittance of which can be controlled by the doping level. A series of samples was synthesized by reactive magnetron sputtering of a metal tungsten target in a mixture of argon, nitrogen and oxygen gases. Warm-colored tungsten oxynitride films were prepared at higher doping levels and characterized using scanning electron microscopy, X-ray diffraction and X-ray photoelectron spectroscopy techniques. Optical properties were measured making use of transmission spectrophotometry and spectroscopic ellipsometry. These extensive experimental studies revealed an increase in absorption towards shorter wavelengths with increasing the doping level. At the same time, it was found that with increasing the doping level, the fraction of non-stoichiometric oxygen also steadily increases to half the total oxygen content. The imperfection of the doped material can stimulate its intercalation with electrolyte ions, accelerating the coloring/bleaching process and increasing the dynamical range between the dark and clear states, thus improving the consumer qualities of electrochemical materials and devices.

**Keywords:** electrochromism; tuhgsten trioxide; nitrogen doping; optical transmittance; spectroscopical ellipsometry

---

## 1. Introduction

Electrochromism of inorganic oxide materials is a phenomenon in which the transparency as well as the color of the material change due to the reversible ion intercalation under the influence of an applied voltage (see [1–8] and references therein). This phenomenon has been known for a long time [9] and has prospects for use in architectural glazing, interior design, and the automotive industry (see [10–17] and references therein), however, it has not yet found mass application, since electrochromic products require long-term stability of many parameters in sometimes harsh operating conditions: high and low temperatures with large gradients, intense exposure to direct sunlight for a long time, etc. Therefore, electrochromic glass is more or less regularly used in the form of rear-view mirrors inside the interior of some brands of cars, window shutters of some aircrafts, etc. There is ongoing work to improve the performance of electrochromic devices, their durability and the number of switches between the colored and bleached states.

Tungsten trioxide $WO_3$ (in general, not fully stoichiometric $WO_{3-x}$) is one of the known cathode electrochromic materials, the optical density of which changes upon intercalation with protons ($H^+$), alkali metal ions (Li,K) and alkaline earth (Al) metals, which are moieties of the electrolyte of an electrochromic cell (see [1–5] and references therein). It can be fabricated in a thin-film form using several techniques such as chemical vapor deposition, physical vapor deposition including reactive sputtering, cathodic electrodeposition and thermal evaporation, wet chemical synthesis including sol-gel processes, hydrothermal and solvothermal methods, electrochemical deposition, spray pyrolysis, deposition of nanoparticles, mechanical sputtering, etc. (see [1,17–21] and references therein). Regardless of the fabrication route, the resulting $WO_{3-x}$ is an inorganic material that is highly resistant to prolonged exposure to sunlight and high temperatures, however, the transition time from the bleached to the colored state and vice versa strongly depends on the method of preparation of tungsten oxide films and can reach several minutes [14,17,18,21]. In addition, the darkened state is characterized by an intense blue color, which is hardly comfortable to potential users of the electrochromic glass technology.

One of the ways to increase the coloring/bleaching rate and its dynamical range could be to redistribute the voltage drop across the anode/electrolyte/cathode stack in favor of the electrolyte. Since, from a formal point of view, tungsten trioxide is a wide-gap semiconductor, its conductivity can be affected by doping. An additional advantage of doping could be the redistribution of the spectral density of light absorption in the relative favor of the short-wavelength (blue) part of the visible spectrum to balance the blue coloration and shift the visual assessment of color towards neutral one (achromatic). Finally, doping can affect the micro- and nanostructure of the tungsten oxide electrode, thus facilitating the process of intercalation/de-intercalation of ions from the electrolyte. Due to the compound nature of the $WO_x$ material, it can be subject to both cationic and/or anionic doping. In this work, we use anionic doping by nitrogen and study the micro- and nanostructure of the resulting tungsten oxynitride material and the behavior of its optical properties when changing the doping level.

## 2. Materials and Methods

Thin films of tungsten oxynitride ($WO_xN_y$ = WON) were grown by reactive magnetron sputtering in an atmosphere of a high-purity reactive plasma gas consisting of argon (plasma-forming gas, flow rate in the range of 80-86 sccm, see Table 1), nitrogen (reactive gas, flow rate 50 sccm) and oxygen (reactive gas, flow rate in the range 4-10 sccm, see Table 1). The pressure was automatically maintained at 4 Pa (30 mTorr) throughout the entire deposition cycle. Sputtering took place from a metal target of high purity tungsten (99.9% of W), the power supplied to the magnetron was automatically maintained constant at a level of 300 W. The substrate for deposition was a polished double-sided glass slide for microscopic studies with a size of 75x25 $mm^2$ and a thickness of 1 mm, pre-cleaned in an aqueous solution of sodium alkylbenzenesulfonate, tetrasodium EDTA and sodium pyrophosphate using an ultrasonic bath. The nomenclature of the synthesized samples is as follows (see Table 1): sample #111 was obtained at an oxygen flow rate of 4 sccm; #092 – with a flow rate of 6 sccm; #091 – with a flow rate of 7 sccm; #082 – with a flow rate of 10 sccm; annealed samples are marked by the suffix “t”, for example #082t.

**Table 1.** Sputtering conditions of the samples and basic properties.

| Sample # | Ar flow rate (sccm) | $N_2$ flow rate (sccm) | $O_2$ flow rate (sccm) | Sputtering pressure (Pa) | Film thickness (nm) [a] | Visible transtmitttance (%) | Film color |
|---|---|---|---|---|---|---|---|
| 111 | 86 | 50 | 4 | 4 | 240 | 20.4 | brown |
| 092 | 84 | 50 | 6 | 4 | 210 | 74.2 | light beige |
| 091 | 83 | 50 | 7 | 4 | 160 | 78.2 | pale yellow |
| 082 | 80 | 50 | 10 | 4 | 120 | 80.6 | transp. blueish |

[a] The typical scatter of the measurement results obtained using a Brooker DectacXT stylus nanoprofilometer with a needle tip radius of 2 μm is about 5 nm.

After evacuating the prepared films from the vacuum chamber, they were cut into several parts for further studies, in particular, one fragment of the each initial sample was collected in an alumina tray and annealed in a muffle furnace in an air atmosphere according to the cyclogram: 2 hours heating from room temperature to 673 K (400°C), then annealing for 10 hours at 673 K and cooling for 4 hours to room temperature.

The morphology of the resulting films was examined using a Carl Zeiss Merlin scanning electron microscope (SEM), while the elemental analysis was carried out using an Oxford Inca energy dispersive X-ray unit (EDX) to a Carl Zeiss EVO50 XVP scanning electron microscope.

X-ray diffraction (XRD) analysis was performed on a Rigaku SmartLab diffractometer with the Cu $K_{\alpha 1}$ radiation ($\lambda$ = 1.5059 Å) in the Bragg-Brentano geometry; the beam incidence angle was 0.3°, the angular step was 0.02° and the scanning speed was 2 seconds per point; range of angles $2\theta$ from 10° to 60°. The diffraction pattern was processed using the built-in PDXL-2 software and the ICDD PDF-2 crystalline compound database.

The near-surface elemental composition and the valence states of constituents were studied by X-ray photoelectron spectroscopy (XPS). The XPS setup operates at a base pressure of $3\text{x}10^{-8}$ Pa, it is equipped with a Mg-$K_{\alpha}$ X-ray source operating at 12.5 kV and 250 W, and a Phoibos 150 hemispherical energy analyzer of photoelectrons (all from SPECS, Berlin). Survey XPS spectra were recorded in the range of 0-1000 eV with an energy step of 1 eV and the pass energy of 80 eV. High-resolution spectra were recorded in limited energy ranges of interest with averaging over 100 scans for all elements, an energy step of 0.1 eV and the pass energy of 20 eV. The setup is also equipped with a built-in option for surface etching with a wide, oblique beam of argon ions of variable energy for depth profiling [22,23].

The optical properties of WON were studied using a Perkin Elmer Lambda 1050 UV/VIS/NIR spectrophotometer in the visible wavelength range of 0.38-0.78 μm in transmission geometry. For more detailed analysis of optical attenuation and refraction, spectroscopic ellipsometry technique (Woollam VASE) was used in the wavelength range of 0.25–2.5 μm in reflection geometry. The measurements were carried out at angles of incidence of the optical axis of collimated radiation of 55° and 75°.

## 3. Results

### *3.1. Scanning Electron Microscopy and X-ray Diffraction (XRD) Analysis*

The morphology of the resulting films was examined using a Carl Zeiss Merlin SEM and showed a mesoporous surface structure of the synthesized samples with dimensional features of two scales: the sub-micron one of about 50–100 nm and predominant much smaller scale in the range mostly below 30 nm (see Figure 1). In particular, the feature size is larger in average for the #111 sample deposited at the minimum oxygen flow rate.

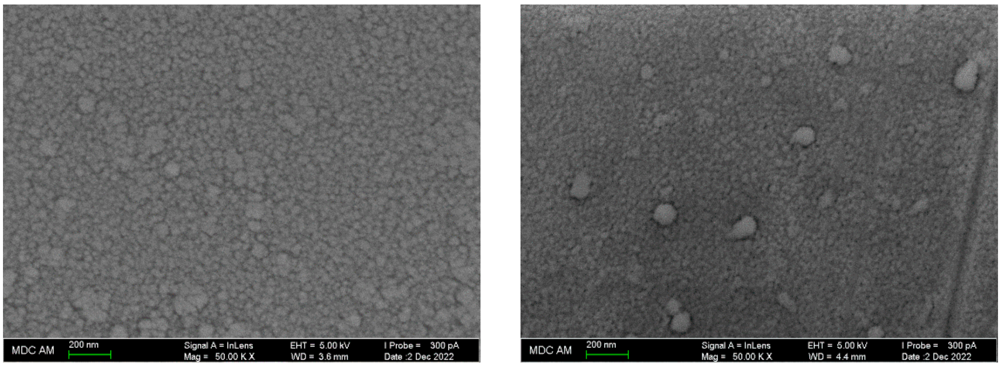

(a) (b)

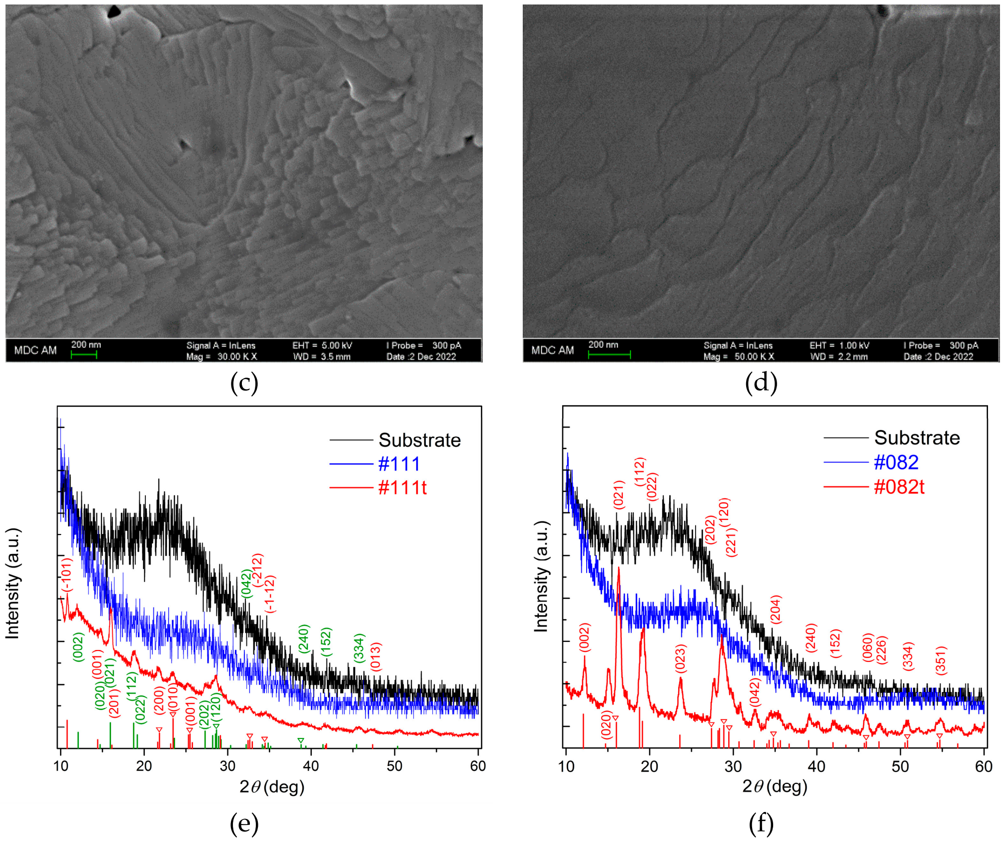

(c) (d)

(e) (f)

**Figure 1.** Scanning electron microscope images of samples #111 (a), #111t (b), #082 (d), #082t (e); X-ray diffraction patterns of samples #111, #111t (c) and #082, #082t (d). The most intense reflections of the 51:49 polycrystalline phases $Na_2W_4O_{13}$ (red labels) and $Na_2W_2O_7$ (green labels) are marked for the #0111t sample (c); the dominant phase of the polycrystalline $Na_2W_2O_7$ phase are marked for the #082t sample (f). The apex-down triangles depict particular reflections in a group which were marked with Miller indices above them.

X-ray diffraction (XRD) analysis performed using the Rigaku SmartLab diffractometer has shown that the glass substrate, generally being an amorphous material, reveals the presence of a short-range order in the arrangement of atoms (broad feature in the range of angles ~ 15-38°). The diffraction pattern of the WON film on the substrate after deposition shows a broad peak of amorphous material with a maximum shifted towards higher angles compared with the substrate. The broad peak of short-range order in the glass substrate is suppressed due to the absorption of X-ray radiation in the film, and the latter broad absorption is a weighted superposition of the absorptions by the film and the substrate.

Peaks appear in the diffraction pattern of the samples after annealing indicating (partial) crystallization of the initially amorphous film material. Moreover, the identification of the crystalline phases shows that the glass substrate ions take part in formation of the crystalline phase. In particular, in sample #111t (~ 240 nm thick film), Figure 1c, the XRD data shows presence of two almost equally weighted crystalline phases, $Na_2W_4O_{13}$ (red labels) and $Na_2W_2O_7$ (green labels) which accumulate a minor portion of the film thickness. A considerable contribution of the amorphous matter indicates this. On the contrary, in sample #082t (~ 120 nm thick), Figure 1f, the XRD data shows dominating crystalline contribution of the phase $Na_2W_2O_7$ which accumulates most of the initial amorphous material of the film. The XRD data indicate that crystallization begins at the film/glass substrate interface.

The elemental composition measured by EDX method has shown the presence of WON film elements, as well as admixture of Na, Ca, Si, characteristic of the glass substrate. It is obvious that the region of excitation of characteristic X-ray radiation by electrons at an accelerating voltage of 10 kV also covers a substrate, since the film is thinner (~ 120–240 nm) than the EDX probing depth of the order of 0.5 µm. Indeed, the third column of Table 2 shows a systematic increase of the oxygen content with decreasing the film thickness from sample #111 to sample #082. Moreover, the W and O columns under the header "Annealed" clearly indicate a gradual increase in the deviation from the $WO_3$ stoichiometry upon going from the thicker to thinner films. Therefore, the tungsten to oxygen ratio should be treated with caution, since the oxygen signal contains a contribution from the substrate (see also a discussion below). Concerning nitrogen content, in the as deposited samples, 4-th column of Table 2, it gradually decreases from ~ 21 at% to ~ 10 at% when the oxygen flow rate increases from 4 sccm, Table 1, sample #111, to 10 sccm, sample #082. Annealing in air leads to the replacement of nitrogen in the film structure by oxygen: the presence of nitrogen is indicated at the level of 2.6 at.% in sample #111t, see 7-th column of Table 2, while for the lower content of nitrogen in the as-deposited samples, #092 to #082, the quantitative definition of nitrogen content is not possible due to the low signal intensity and the overlap of the nitrogen line with the lines of oxygen and calcium.

**Table 2.** Elemental composition of the samples according to EDX data (only results for W,O and N are shown, averaged over three sampling points for the each sample).

| | **As deposited (at.%)** | | | **Annealed (at.%)** | | |
|---|---|---|---|---|---|---|
| **Sample #** | W | O | N | W | O | N |
| 111 | 20.2 | 58.8 | 21.0 | 19.4 | 78 | 2.6 |
| 092 | 12.4 | 76.2 | 11.4 | 15.3 | 84.7 | - |
| 091 | 10.1 | 80.8 | 9.1 | 12.0 | 88.0 | - |
| 082 | 7.2 | 82.9 | 9.9 | 4.5 | 95.5 | - |

### *3.2. X-ray Photoelectron Spectroscopy*

The XPS method also makes it possible to estimate the elemental composition of the material being probed, however, the advantage of the XPS method lies in the possibility of determining the valence composition of material under study. Unlike the EDX method, XPS is intended for surface and near-surface studies, since the probing depth is several nanometers. It is obvious, that the substrate does not contribute to the signal from the film with a thickness of 120–240 nm, however, surface contaminations, for example, with carbon dioxide from air, and gradual oxidation of the surface at ambient conditions may lead to extrinsic contributions to the XPS signal (see below).

Figure 2 shows the overview XPS spectra of samples #111 and #082, as well as the high-resolution spectra separately for W, O, and N (see the figure caption). The results of the valence analysis are presented element by element in Table 2. The XPS spectrum of tungsten contains one or two doublets with binding energies of 35.8 eV and 37.9 eV, and 34.3 eV and 36.4 eV, respectively. The binding energies of the more intense doublet of 35.8 eV and 37.9 eV in sample #111, Figure 2b, correspond to tungsten in the 6+ valence state [24–26], while the binding energies of the less intense doublet are attributed to tungsten in a non-stoichiometric environment (partially reduced) [24,25]. In sample #082, tungsten was found only in the oxidized state 6+ (see Figure 2f).

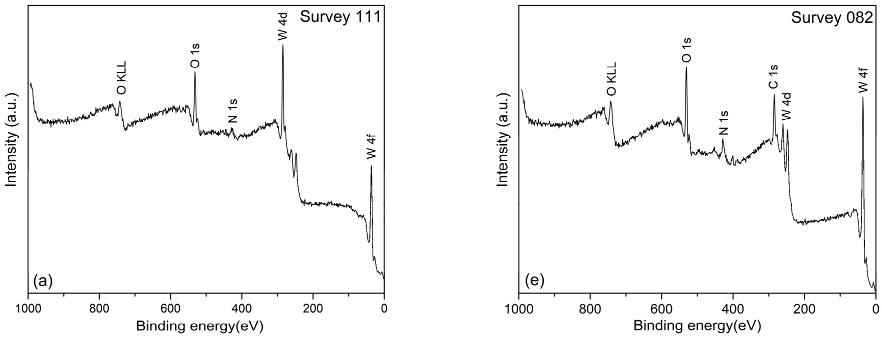

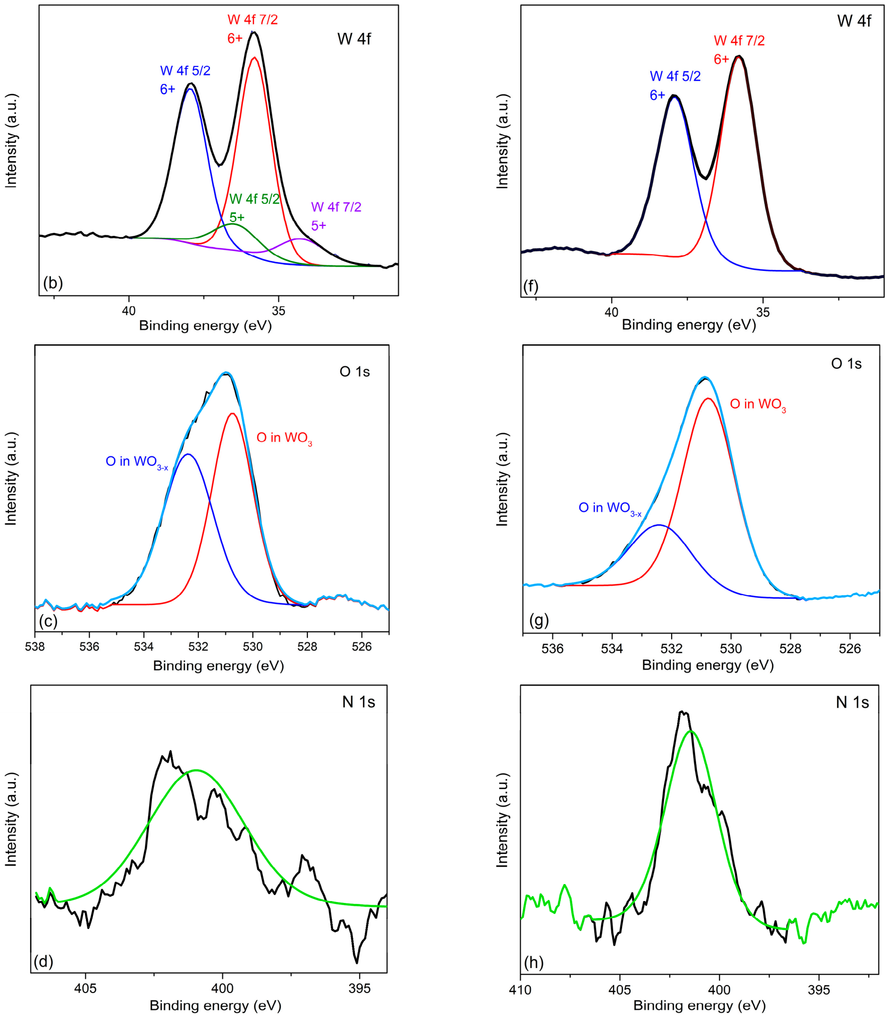

**Figure 2.** XPS measurement results. Left column – sample #111, right column – sample #082: (a)/(e) survey spectrum showing the contributions of all elements present in the #111/#082 film; (b)/(f) high-resolution spectrum of the tungsten 4f transitions along with their decomposition into valence contributions; (c)/(g) high-resolution spectrum of the oxygen 1s transitions along with its decomposition into bonding-dependent contributions; (d)/(h) high resolution spectrum of the nitrogen 1s transitions approximated by the Lorentz-Gaussian lineshape (light-green lines).

The nitrogen lines have a low signal-to-noise ratio, therefore, identification of valence states was not carried out. Due to the small depth of probing, the nitrogen to oxygen signal ratio should be treated critically, since after evacuation from the vacuum chamber, the non-equilibrium oxidized tungsten, located close to the film surface, continues oxidizing by atmospheric oxygen. Due to the shallow probing depth, a sizeable contribution to the oxygen XPS signal is made by near-surface oxygen chemisorbed from the ambient atmosphere, which leads to an overestimation of its content.

To get rid of the surface oxygen signal, we used the built-in option of the surface etching with a wide oblique beam of argon ions. To be sure that the etching rate does not depend noticeably on the presence of nitrogen, we etched the #111 sample comparatively with pilot sample #082t, in which tungsten is completely oxidized to a valence of 6+, and the presence of nitrogen is not detected by any methods available to us. As a result, we got almost identical evolution of the W and O XPS spectra for both samples, but the intensity of the nitrogen signal in the #111 sample quickly increased and saturated at a level four times higher than for the non-etched state. This indeed indicates oxidation of the surface of sample #111.

An additional information can be obtained from analysis of the oxygen signal lineshape, Figure 2c,g, showing the splitting of the XPS line into two components. One of them (with a binding energy of 530.8 eV) is identified as stoichiometric oxygen in the composition of $WO_3$ [24,25], while the other with a binding energy of 532.4 eV is identified as oxygen in the nonstoichiometric tungsten oxide. Analysis of the experimental data for all samples has shown (see Table 3) that in the non-annealed samples the fraction of the non-stoichiometric oxygen (third column of the Table 3) steadily increases with increasing the nitrogen content.

**Table 3.** Dependence of stoichiometric and non-stoichiometric fractions of oxygen on the nitrogen content in the as-deposited and annealed samples (each is averaged over 3 sampling points).

| | **As deposited** | | **Annealed** | |
|---|---|---|---|---|
| **Sample #** | O 1s (530.7 eV) | O 1s (532.2 eV) | O 1s (530.8 eV) | O 1s (532.5 eV) |
| 111 | 53 | 47 | 68 | 32 |
| 092 | 61 | 39 | 72 | 28 |
| 091 | 62 | 38 | 70 | 30 |
| 082 | 72 | 28 | 62 | 38 |

*3.3. Spectrophotometric Measurements*

Figure 3 shows photographs of the as-deposited samples (top row, (a) to (d)) and the results of the spectroscopic transmission measurements (window (e)). Visually, sample #111 is brown; sample #092 – light beige; sample #091 – light yellow; sample #082 - transparent with a bluish tint. The integral transmission in the wavelength range of 0.38-0.78 μm is 20.4%, 74.2%, 78.2% and 80.6% for samples #111, #092, #091 and #082, respectively (see Table 1).

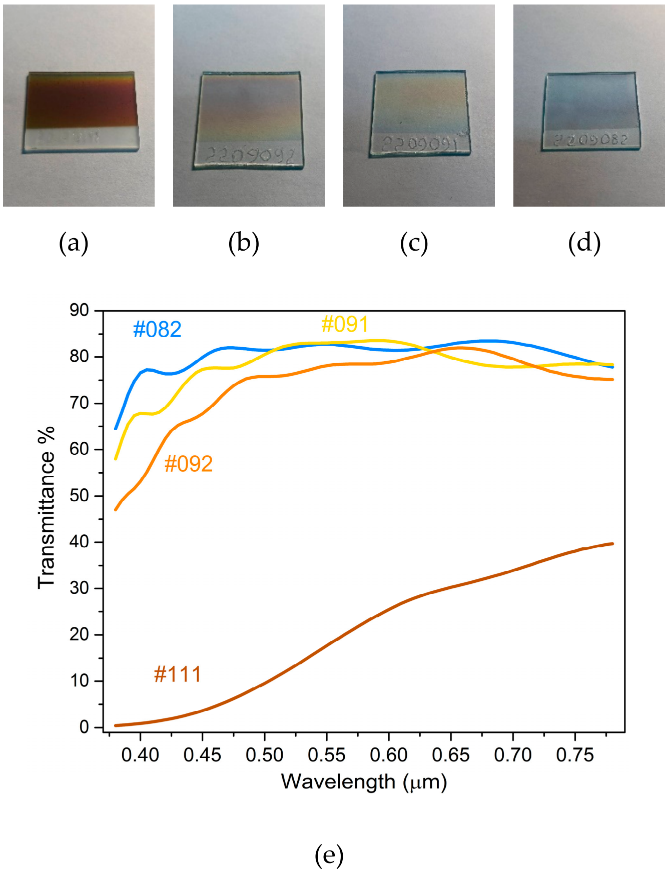

(a) (b) (c) (d)

(e)

**Figure 3.** (a-d) Images of samples #111 ($O_2$ flow rtae – 4 sccm), #092 ($O_2$ – 6 sccm), #091 ($O_2$ – 7 sccm) and #082 ($O_2$ – 10 sccm). (e) Dependence of transmittance on the wavelength in the visible range of light.

*Preprints* (www.preprints.org) | NOT PEER-REVIEWED | Posted: 28 November 2023 doi:10.20944/preprints202311.1755.v1

The optical transmission spectrum of the samples is presented in panel (e) of Figure 3. The oscillatory component of the absorption dispersion for samples #082, #091 and #092 originates from the light interference in a thin semi-transparent film. It can be seen that for sample #111 with the maximum nitrogen content, the transmission is minimal in the short wavelength side; it monotonically increases towards the long wavelengths from almost zero to ~ 40%. The lack of transmission of blue and green colors leads to severe darkening of the WON film. Increasing the oxygen flux during the film deposition from 4 to 6 sccm with a constant nitrogen flux of 50 sccm (see Table 1) leads to sharp changes in optical transmission, significantly increasing transparency in the short-wavelength part of the spectrum with a rough constant absorption at longer wavelengths. As a result, the intensity of the brown color drops down significantly, turning the film color into light-beige. A further increase in the oxygen flow rate to 7 sccm leads to a color change to yellow due to an increase in transmittance in the wavelength range of 0.38-0.635 μm, with approximately the same transmittance at longer wavelengths. Finally, increasing the oxygen flow rate to 10 sccm increases transmittance in the wavelength range of 0.38-0.505 μm, while approximately maintaining transmittance at longer wavelengths. It is observed as a blue tint of light transmitted by the sample. Thus, we observe that the anionic doping of tungsten oxide with nitrogen leads to the appearance of a warm coloration of the resulting tungsten oxynitride film.

### *3.4. Spectroscopical Ellipsometry*

Extended information about the optical properties of tungsten oxynitride can be obtained from spectrometric ellipsometry measurements in the wavelength range of 0.25-2.5 μm. The measurement results are presented in Figure 4 in the form of the dependence of the refraction *n* and extinction *k* coefficients on the wavelength of the incident radiation. They show that the anionic doping with nitrogen leads to a systematic increase in absorption in the short-wavelength region, which leads to the dominance of long waves in transmission and, as a consequence, to the coloration of the nitrogen-doped tungsten oxide layer to warm colors.

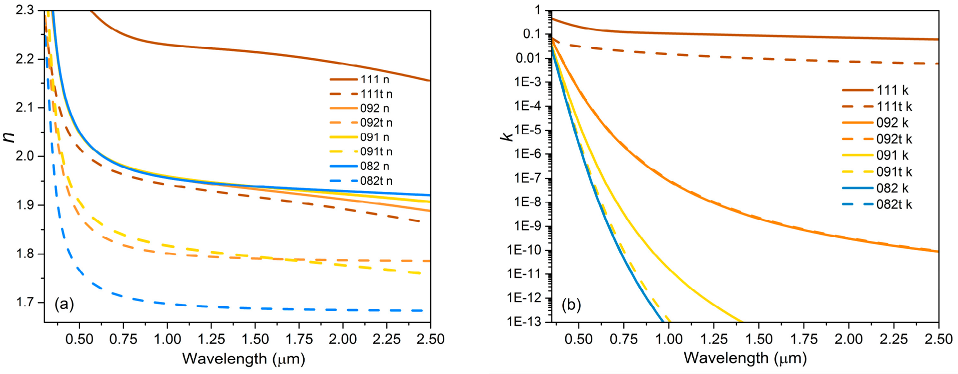

(a) (b)

**Figure 4.** Spectroscopic ellipsometry results: (a) dependence of the refraction coefficient *n* on wavelength; (b) dependence of the extinction coefficient *k* on wavelength.

## 4. Discussion

The article considers anionic doping of the cathode electrochromic material tungsten trioxide by nitrogen. Visually, with increasing doping level, the effect of coloring in warm colors was observed – from transparent bluish to brown, through yellow and beige shades. XRD measurements have shown that predominantly amorphous films of tungsten oxynitride were deposited (Figure 1c,f, blue lines) with a broad shoulder in the angle range of 18-38°. It is most likely a reminiscense of the most intense reflections of $WO_3$ crystalline powder structure [27], generated by the short-range order in the quasi-amphibious film. Upon annealing, the films partially crystallize (Figure 1c,f, red lines) with rising up XRD peaks corresponding to the crystalline powder reflections of $Na_2W_4O_{13}$) and $Na_2W_2O_7$ compounds for the thickest #111t sample; and $Na_2W_2O_7$ compound for the thinnest #082t sample. The crystalline phases of the #111t sample accumulate only minority of the total initial film volume, while the crystalline phase of the #082t sample accumulates the majority of the film volume (see red lines in Figure 1c,f). This observation gives a clear hint that crystallization starts from the substrate-film interface. The significantly increased contribution of stoichiometric oxygen to the XPS spectra in all samples upon annealing, see Table 3, two columns in the right, occurs because of nitrogen escape (see Table 2) as well as general increase of order upon annealing. Ultimately, the annealed films become transparent which is characteristic to stoichiometric tungsten oxide compounds with the available elements from our samples.

The study of optical properties by the transmission spectrophotometry and spectroscopic ellipsometry has shown that anionic doping of tungsten trioxide with nitrogen leads to an increase in absorption at short (UV) wavelengths without noticeable modification at wavelengths above ~ 0.6 μm, at least up to 2.5 μm which is the limit of our spectrometers. This short-wavelength absorption causes the material to have warm colors, in contrast to the dark-blue coloration of tungsten trioxide itself upon intercalation with Li.

An intriguing conclusion can be drawn from the systematic increase of the fraction of non-stoichiometric oxygen with increasing the nitrogen doping level (Table 3, third column). It is known that the amorphous character of $WO_{3-x}$ films as well as imperfections like oxygen vacancies enhance coloration efficiency [8,21,28,29]. Therefore, nitrogen-doped tungsten oxide material can color/bleach deeper and faster, opening up directions for improving the consumer properties of electrochemical materials and devices.

**Author Contributions:** Conceptualization, L.T. and M.S.; methodology, L.T. and M.S.; sample preparation, I.M.; investigation, I.M, N.L., M.S., and L.T.; resources, L.T. and M.S.; data curation, I.M, N.L., and L.T.; writing—original draft preparation, L.T.; writing—review and editing, M.S., I.M., N.L.; visualization, I.M.; supervision, L.T.; project administration, L.T.; funding acquisition, L.T. All authors have read and agreed to the published version of the manuscript.

**Funding:** The research of I.M., N.L. and L.T. was funded by RSF, project # 22-22-00980.

**Data Availability Statement:** The data presented in this study are available on request from the corresponding author.

**Acknowledgments:** The authors sincerely thank V. Meshcheryakov, V. Chugunov, M. Yermakov, R. Batulin, A. Gumarov, L. Nurtdinova, A. Rogov, I. Tverdov, I. Vakhitov, and R. Yusupov for their valuable support in sample preparation and measurements. X-ray diffraction studies were carried out using the equipment of the Center for Shared Facilities “Nanomaterials and Nanotechnologies” of the Kazan National Research Technological University (KNRTI - KChTI).

**Conflicts of Interest:** The authors declare no conflict of interest.

## References

1. Granqvist C.G. *Handbook of Inorganic Electrochromic Materials*, Elsevier, 2002, 663 p.
2. Monk, P.M.S.; Mortimer,R.J.; Rosseinsky, D.R. *Electrochromism and Electrochromic Devices*. Cambridge University Press: Cambridge CB2 8RU, UK, 2007; 483 p. www.cambridge.org/9780521822695.
3. Niklasson, G.A.; Granqvist, C.G. Electrochromics for Smart Windows: Thin Films of Tungsten Oxide and Nickel Oxide, and Devices Based on These. *J. Mater. Chem*. **2007**, *17*, 127–156. DOI:10.1039/B612174H.
4. He, T.; Yao, J. Photochromic Materials Based on Tungsten Oxide. *J. Mater. Chem*., **2007**, *17*, 4547. DOI: 10.1039/B709380B.
5. Gillaspie, D.T.; Tenent, R.C.; Dillon, A.C. Metal-oxide films for electrochromic applications: present technology and future directions. *J. Mater. Chem*. **2010**, *20*, 9585–9592. DOI: 10.1039/c0jm00604a.
6. Ma, D.; Wang, J. Inorganic electrochromic materials based on tungsten oxide and nickel oxide nanostructures. *Sci. China Chem*. **2017**, *60*, 54–62. DOI:10.1007/s11426-016-0307-x.
7. Maiorov, V.A. Electrochromic Glasses with Separate Regulation of Transmission of Visible Light and Near-Infrared Radiation (Review). *Optics and Spectroscopy* **2019**, *126*, 412–430. DOI: 10.1134/S0030400X19040143.
8. Li, Z.; Liu, Zh.; Zhao, L.; Chen, Y.; Li, J.; Yan, W. Efficient electrochromic efficiency and stability of amorphous/crystalline tungsten oxide film. *Journ. Alloys and Comp*. **2023**, *930*, 167405. DOI: 10.1016/j.jallcom.2022.167405.
9. Deb, S.K. A novel electrophotographic system. *Applied Optics* **1969**, *8*(S1), 192-195. DOI:10.1364/AO.8.S1.000192.

10. Granqvist, C.G.; Lansaker, P.C.; Mlyuka, N.R.; Niklasson, G.A.; Avendano, E. Progress in chromogenics: New results for electrochromic and thermochromic materials and devices. *Sol. Energy Mater. Sol. Cells* **2009**, *93*, 2032-2039, doi.org/10.1016/j.solmat.2009.02.026.
11. Granqvist, C.G.; Green, S.; Niklasson, G.A.; Mlyuka, N.R.; Kraemer, S.; Georen, P. Advances in chromogenic materials and devices, *Thin Solid Films* **2010**, *518*, 3046-3053, DOI:10.1016/j.tsf.2009.08.058.
12. Granqvist, C.G. Electrochromics and Thermochromics: Towards a New Paradigm for Energy Efficient Buildings. *Mater. Today: Proc.*, **2016**, *3*, S2–S11. DOI: 10.1016/j.matpr.2016.01.002.
13. Shchegolkov, A.V.; Tugolukov, E.N.; Shchegolkov, A.V. Overview of Electrochromic Materials and Devices: Scope and Development Prospects, *Advanced Materials and Technologies* **2020**, N2(18), 66-73. DOI: 10.17277/amt.2020.02.pp.066-073.
14. Zhang, Wu; Li, H.; Hopmann, E.; Elezzabi, A.Y. Nanostructured inorganic electrochromic materials for light applications, *Nanophotonics* **2020**, *10*, 825–850. DOI: 10.1515/nanoph-2020-0474.
15. Shchegolkov, A.V.; Parfimovich, I.D.; Komarov, F.F.; Shchegolkov, Al-der V.; Tugolukov, E.N. Optically Adjustable Nanocomposite Electrochromic Film $WO_3$/rGO to Control Light Transmission and Protect from Electromagnetic Radiation. *Inorg. Materials: Appl. Research*, **2021**, *12*, 1547–1553. DOI: 10.1134/S207511332106023X.
16. *Eco-efficient Materials for Reducing Cooling Needs in Buildings and Construction. Design, Properties and Applications*, Edited by F. Pacheco-Torgal, L. Czarnecki, A.L. Pisello, L.F. Cabeza, C.-G. Granqvist, Elsevier, 2021, 469 p.
17. Shchegolkov, A.V.; Jang, S.-H.; Shchegolkov, A.V.; Rodionov, Y.V.; Sukhova, A.O.; Lipkin, M.S. A brief overview of electrochromic materials and related devices: A nanostructured materials perspective. *Nanomaterials* **2021**, *11*, 2376. DOI: 10.3390/nano11092376.
18. Park, S.-I.; Quan, Y.-J.; Kim, S.-H.; Kim, H.; Kim, S.; Chun, D.-M.; Lee, C.S.; Taya, M.; Chu, W.S.; Ahn, S.-H. A review on fabrication processes for electrochromic devices, *Int. J. Pr. Eng. Man.-GT* **2016**, *3*, 397-421. DOI: 10.1007/s40684-016-0049-8.
19. Jittiarporn, P.; Badilescu, S.; Al Sawafta, M.N.; Sikong, L.; Truong, V.-V. Electrochromic properties of sol-gel prepared hybrid transition metal oxides – A short review, *J. Sci.-Adv. Mater. Dev.* **2017**, *2*, 286-300. DOI: 10.1016/j.jsamd.2017.08.005.
20. Shchegolkov, A.V.; Knyazev, L.G.; Shchegolkov, A.V.; Komarov, F.F.; Parfimovich, I.D. A Study of the $WO_3$/GO Electrochromic Films Obtained by the Electrochemical Deposition Route: Optical and Electromagnetic Method. *Russian Journal of General Chemistry*, **2021**, *91*, No. 12, pp. 2660–2666. DOI: 10.1134/S1070363221120392.
21. Zeb, Sh.; Sun, G.; Nie, Y.; Xu, H.; Cui, Y.; Jiang, X. Advanced developments in nonstoichiometric tungsten oxides for electrochromic applications, *Mater. Adv.*, **2021**, *2*, 6839-6884. DOI: 10.1039/D1MA00418B.
22. Esmaeili, A.; Yanilkin, I.V.; Gumarov, A.I.; Vakhitov, I.R.; Gabbasov, B.F.; Kiiamov, A.G.; Rogov, A.M.; Osin, Y.N.; Denisov, A.E.; Yusupov, R.V.; et al. Epitaxial Growth of $Pd_{1-x}Fe_x$ Films on MgO Single-Crystal Substrate. *Thin Solid Films* **2019**, *669*, 338–344, doi:10.1016/j.tsf.2018.11.015.
23. A.I. Gumarov, I.V. Yanilkin, R.V. Yusupov, A.G. Kiiamov, L.R. Tagirov, R.I. Khaibullin, Iron-implanted epitaxial palladium thin films: Structure, ferromagnetism and signatures of spinodal decomposition. *Mater. Lett*. **2021**, *305*, 130783. DOI: 10.1016/j.matlet.2021.130783.
24. Bouvard, O.; Krammer, A.; Schüler, A. In situ core-level and valence-band photoelectron spectroscopy of reactively sputtered tungsten oxide films. *Surf. Interface Anal.* **2016**, *48*, 660-663. DOI 10.1002/sia.5927.
25. Yang, B.; Miao, P.; Cui, J. Characteristics of amorphous $WO_3$ thin films as anode materials for lithium-ion batteries. *J Mater Sci*: *Mater Electron* **2020**, *31*, 11071–11076. DOI: 10.1007/s10854-020-03656-5
26. Nguyen, H.T.T.; Truong, T.H.; Nguyen, T.D. et al. Ni-doped $WO_3$ flakes-based sensor for fast and selective detection of $H_2S$. *J Mater Sci: Mater Electron* **2020**, *31*, 12783–12795. DOI: 10.1007/s10854-020-03830-9
27. http://database.iem.ac.ru/mincryst/s_carta.php?OXIDE_W+3412
28. Lee, S.-H.; Cheong, H.M.; Tracy, C.E.; Mascarenhas, A.A.; Czanderna, W.; Deb, S.K. Electrochromic coloration efficiency of a-$WO_{3-y}$ thin films as a function of oxygen deficiency. *Appl. Phys. L;ett.* **1999**, *75*, 1541-1543. DOI: 10.1063/1.124782.
29. Vernardou, D.; Parkin, I.P.; Drosos, C. Chemical vapor deposition of oxide materials at atmospheric pressure. *Handbook of Modern Coating Technologies* **2021**, 101-119. DOI: 10.1016/B978-0-444-63240-1.00004-8.